REPORT DOCUMENTATION PAGE

Form Approved
OMB NO. 0704-0188

1. AGENCY USE ONLY *(Leave blank)*	2. REPORT DATE	3. REPORT TYPE AND DATES COVERED
		Final Report 15Jun93 - 30Sep97

4. TITLE AND SUBTITLE

Ferroelectric Heterostructures Materials Development, Modeling & Testing

5. FUNDING NUMBERS

6. AUTHOR(S)

Andrew Peter Jardine

DAAH04-93-G-0213

7. PERFORMING ORGANIZATION NAMES(S) AND ADDRESS(ES)

State University of New York at Stony Brook
Stony Brook, NY 11794-3362

8. PERFORMING ORGANIZATION REPORT NUMBER

9. SPONSORING / MONITORING AGENCY NAME(S) AND ADDRESS(ES)

U.S. Army Research Office
P.O. Box 12211
Research Triangle Park, NC 27709-2211

10. SPONSORING / MONITORING AGENCY REPORT NUMBER

ARO 32114.1-MS-SM

11. SUPPLEMENTARY NOTES

12a. DISTRIBUTION / AVAILABILITY STATEMENT

Approved for public release; distribution unlimited.

12 b. DISTRIBUTION CODE

13. ABSTRACT *(Maximum 200 words)*

A materials development effort has been conducted to explore the feasibility of constructing ferroeleatic-ferroelectric heterostructures that could be used to dampen shock waves. The original concept proposed to use a thin film of PZT on the front surface to act as a sensor to detect the pressure pulse. TiNi, in both thin-film form and as a porous metal, would be incorporated into the structure to passively damp the stress wave. Finally, another layer of PZT would be introduced to actively damp the pulse by applying a counter pulse. This program investigated aspects of the materials synthesis and interface engineering needed to integrate TiNi and PZT into a single device.

20000628 024

14. SUBJECT TERMS			15. NUMBER IF PAGES
			16. PRICE CODE

17. SECURITY CLASSIFICATION OR REPORT	18. SECURITY CLASSIFICATION OF THIS PAGE	19. SECURITY CLASSIFICATION OF ABSTRACT	20. LIMITATION OF ABSTRACT
UNCLASSIFIED	UNCLASSIFIED	UNCLASSIFIED	UL

FINAL PROGRESS REPORT

1. ARO Proposal Number: DAAH04-93-G0213.
2. Period Covered by Report: 6/15/93-9/30/97
1. Title of Proposal: Ferroelastic-Ferroelectric Heterostructures
2. Contract or Grant Number: DAAHO4-93-G-0213

5. Name of Institution: State University of New York at Stony Brook
6. Author of Report: Dr. Andrew Peter Jardine
7. List of Manuscripts submitted or published under ARO sponsorship during this period, including Journal references:

FINAL PROGRESS REPORT

Foreword

" Ferroelastic Ferroelectric Heterostructures" was an initial study to synthesize a truly smart material, in which sensing, actuation and control were built into a material heterostructure such the minimal interfacing to an external control system was required. The premise for the device was that shock damping could be enhanced using a combination of PZT and TiNi. Thin Film PZT was used as a sensor to detect a pressure pulse. TiNi was used as both as a thin film and a porous metal to passively damp a stress wave and a final layer cf PZT was used to actively damp the pulse by applying a counter pulse into the TiNi. Research into the device focussed on growth mechanisms for combining TiNi and PZT and learning the processing involved to grow TiNi porous metals for the device.

The initial Principal Investigator was Prof. Peter Jardine, and in the 1.5 years that he held the grant, thin film TiNi/PZT heterostructures were developed as were the growth mechanisms for TiNi porous metals. Unfortunately, key senior faculty at the Materials Science and Engineering Dept. at SUNY Stony Brook was hostile to this research and the Dean offered no support for this research, and as a result Jardine left to join Northrop Grumman in 1995. Transfer of the grant to Prof. John Parise occurred, who is an expert in sol-gel processing. The majority of the research into thin film TiNi development occurred under the auspices of Prof. Carman's group at UCLA, with guidance from Jardine in the capacity of a visiting Professor in the Dept. of Mechanical and Aerospace Engineering at UCLA.

As a result of the transfer, some focus in the development of the device was lost. Redirection of the grant, with ARO approval occurred, consequently the UCLA work focussed largely on thin film TiNi actuators. However, despite the transfer, we were able to show that such shock damping heterostructures are possible to fabricate. It remains to be seen how effective these devices are in a shock environment, and this evaluation is necessary in order to extract a meaningful message from the work described below.

(2) Table of Contents (if more than 10 pages)

(3) List of Appendixes, Illustrations and Tables (if applicable)

(4) Statement of the problem studied:

Damping of shock waves via an intriniscally smart combination of damping materials is possible using PZT and TiNi combined as a heterostructure. The program studied methods to synthesize these materials such that an evaluation of the damping characteristics could eventually occur.

2

(5) Summary of the Results:

1-Introduction

Smart active damping of mechanical vibrations is a possible application for these heterostructures. This requires the heterostructure to be able to sense the incoming stress wave and to actively respond. The logic of active damping by a ferroelastic-ferroelectric structure can be explained by considering an approaching stress wave shown in Figure 1-1. The stress wave propagates into the TiNi producing a martensitic-austenitic phase transformation in which some of the mechanical energy is converted to heat. This layer is designed to absorb most of the high energy waves. Acoustic waves that are not damped by the TiNi layer continue to propagate and strain the first ferroelectric layer (PZT). This strain produces a voltage through the direct piezoelectric effect which can be used to generate an out of phase stress wave by the second ferroelectric layer to attenuate any remaining stress waves. By varying the buffer layer (i.e., TiO_2) between the ferroelectric layers, it is possible to control the resistance and capacitance of the resulting circuit. To account for the possibility of the velocity of the stress wave to exceed the system's response time, a metallic mechanical impedance buffer (such as Al, Ti and TiNi) can be added to provide additional time for the counter-stress actuation to occur.

This work is divided into several sections based on the material science that was required to engineer the interfaces within the ferroelectric-ferroelastic heterostructure (FFH). The materials themselves are well known, comprising TiNi and PZT, however their synthesis into the FFH was not known previously. The materials synthesis routes that were developed included,
- Thin film TiNi,
- PZT/TiNi,
- Porous TiNi,

and this is how the report is divided.

To investigate the growth mechanisms of PZT/TiNi, a smooth well-characterized surface was required. TiNi thin films were chosen as the sputter deposition process of TiNi was known from the authors previous work, but largely that a large number of sample surfaces could be generated cheaply, as opposed to cutting and grinding and polishing expensive TiNi boules. Sputter deposition also allowed for selectively varying the composition of the TiNi and so there were many advantages in pursuing this line of attack in the investigation.

Once we established growth and processing conditions for thin film TiNi, development of the TiNi/PZT interface was accomplished using TiNi thin films on quartz or silicon, and PZT thin films were grown using sol-gel techniques. After successful processing of the PZT thin film on TiNi, the PZT was poled and ferroelectric characterization curves were obtained to judge the quality of the film.

3

It has long been understood that porous and foamed materials are effective in shock damping. It was also understood that TiNi has good shock damping capabilities in its own right from cavitation-erosion studies. Porous TiNi did not exist at the time, and so efforts were spent there to generate porous TiNi from elemental Ti and Ni powders. TiNi powders were found to be extremely expensive, and using Ti and Ni reduced the cost of the final structure by over a factor of 10.

At this point in the investigation, the grant was effectively transferred to UCLA, where more detailed characterization of the TiNi thin films occurred. This was for two reasons: Prof. Carmans' group had similar interests in smart materials systems and had significant research with ARO, and that there was no one competent in smart materials at Stony Brook. Prof. Parise is a well recognized expert in sol-gel synthesis and he graciously agreed to be caretaker for the research. These program changes were agreed to by ARO.

2-Thin Film Deposition of TiNi

Sputter deposition of TiNi has been problematic due to the extreme reactivity of titanium. There are several advantages in depositing TiNi with other metals, such as Ti and Cu, as the Shape Memory Effect properties can be changed selectively, including coring of the thin film. Simultaneous co-deposition of cored material using sputter deposition becomes technically difficult as this implies that the sample to target distance increases. In this paper, we discuss a relationship developed so that a basic base vacuum pressure can be found with target-sample distance and correlated with the observed phases for both Ti and TiNi samples. Practical limitations imposed by the vacuum system on both devices and device quality are discussed.

2-1 Introduction

The Shape Memory Effect (SME) is associated with dramatic, temperature dependent mechanical properties, resulting from a first order martensitic phase transformation from a high symmetry, high temperature *austenitic* phase to a low symmetry, low temperature *martensitic* phase. The low temperature phase is easily twinned into many crystallographic twin variants, with one crystallographic twin growing at the expense of the others with an applied stress. On heating, the twins revert to their original configuration on transformation into the austenitic phase. Macroscopically, the martensitic material is easily deformed through the growth of these twins, which can accommodate seemingly plastic true strains (of up to 8% for TiNi). These strains are recovered on heating through its transformation into its high temperature phase and shape, hence the term the Shape Memory Effect.

The intermetallic TiNi is a commonly used SME alloy. Crystallographically, the martensitic transformation is from the high temperature, austenitic bcc B2 phase to the lower temperature, martensitic monoclinic B19' phase. Its selection as the alloy of choice is due to its excellent material properties, including strong recovery forces, a

4

transformation above room temperature for the stoichiometric composition, excellent corrosion-resistance and environmental inertness. Difficulties in further exploiting SME TiNi result from a large exothermic heat of transformation which limits the cycle lifetime as well as poor machineability, which limits its ability to be used in many applications.

Thin film TiNi up to 20 µm thick have been developed using either DC or RF Magnetron sputtering [2-1,2-2,2-3,2-4,2-5] and the related technique of ion-sputter deposition and Ion Beam Assisted Deposition (IBAD) processing [2-6] onto a variety of substrates such as: Si, GaAs, CdS, SiO_2 and NaCl. In all cases, base pressures for sputtering were in the range of 10^{-7} torr, with sputtering at higher base pressures of 10^{-6} torr generally not producing TiNi films. As thin films, there is a small thermal mass to heat and cool, resulting in fast cycling times. When grown on Si, a good heat conductor, good thermal coupling results which further decreases the cycling time[2-7]. When deposited onto flat substrates, the material can be patterned using standard lithographic techniques.

Although still in its infancy, there are growing technical applications for thin film TiNi in Micro-Electro Mechanical Machines (MEMS) applications. Patents and commercial products for valves as well as in biomedical applications have also been developed[8]. Of some interest is thus the manufacturability of these thin films and in particular the consistency of the TiNi's Shape Memory Effect properties over the substrate wafer.

There are several problems associated with DC sputter deposition. As seen in Figure 2-1, although the TiNi alloy is largely a stoichiometric intermetallic, there can exist small compositional deviations, with large changes in the resultant transformation temperatures [2-9]. Thus, small changes in composition, such as being outside of the DC sputtering plume, can result in large changes to the thermo-mechanical properties of the alloy.

In this paper, an attempt to quantify the compositional differences imposed by the change in sample to target distance is discussed and related to X-ray Diffraction (XRD) observations of TiNi thin films deposited on quartz substrates.

2-2 Calculation

As mentioned above, the dominant issue involved in determining the quality of the thin films is the extreme reactivity of the Ti atoms, which bind with reactive gas species to produce stable oxide and nitride species. As a consequence, the net stoichiometry of the Ti-Ni thin film changes, with the aforementioned dramatic changes in the transformation temperatures associated with the SME.
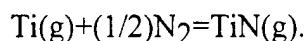
For the purposes of an amenable calculation, it is taken that the probability of a Ti atom colliding with reactive gas species, such as oxygen, water vapor or nitrogen, *and subsequently reacting to form stable gaseous molecules will be unity*, such as by the reaction

$$Ti(g) + O_2(g) = TiO_2(g),$$

or

$$Ti(g)+ H_2O(g)=TiO(g) +H_{2(g)},$$

or

$$Ti(g)+(1/2)N_2=TiN(g).$$
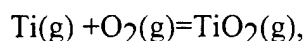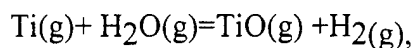
This assumption is reasonable considering the highly negative enthalpies of formation for these compounds. Thus, to avoid changes in stoichiometry, the collision probabilities with these species must be kept low.

Typical Argon sputtering pressures are of the order of 2 to $5x10^{-3}$ torr, which corresponds to a mean free path of any atom of 0.25 cm[10]. If the Ti-Ar interaction is ideal, with elastic collisions, then one can easily simulate the random walk of an Ti atom and thereby calculate the average number of collisions that an atom will experience in moving from the target to the sample. The number of collisions is important as it directly relates to the probability of a Ti atom colliding with a reactive contaminant.

The probability of an event not happening N times is P, where
$$P=(P_r)^N,$$
and P_r is the probability of the event not happening once. In this case, P_r is related to the relative vapor pressure of the reactive contaminants (P_{cont}) as compared to the total vapor pressure (P_{tot}). As per Dalton's Law of Partial Pressures, then
$$P_r=P_{cont}/P_{tot}$$
Referring to Figure 1, an obvious benchmark for a successful TiNi deposition is the degree to which stoichiometry is maintained. If a 1 at.% deviation is allowable, (corresponding to practical limit of these materials as actuators), this implies that one in 100 Ti atoms can react with the gas contaminants and therefore
$$P=0.01$$
This value would then imply that a stoichiometric TiNi target would be deposited as a 51 at.% Ni-Ti thin film. As the transformation temperatures are highly dependent upon stoichiometry, this would imply significant crease in transformation temperature. A more reasonable value for the collision probability of
$$P=0.001$$
would mark the upper bound, as this would therefore generate a small net offset in stoichiometry of 50.1 at.% Ni.

The calculation of N vs. d was based on simulation, where the Ti atom starts at a given trajectory normal to the target surface, and collides after one mean free path length. As the collisions are elastic, the next trajectory is based on a random selection from $0°$ to 360°. (Since the sample-target sputtering geometry is cylindrically symmetric, the calculation can be reduced to a planar geometry.) The number of collisions was recorded for the Ti atom to migrate from the target to the sample. This process was repeated 100 times and an average number of collisions calculated. This average number of collisions was then related to the maximum base pressure using Dalton's law, with the sputtering pressure set at P=2 mTorr.

The average number of collisions was found to increase significantly with increasing target to sample distance. Figure 2 shows the corresponding base pressure for a given

probability of collision and total pressure of 2 mTorr. For a P_r value of 0.01, representing the lower limit, at a distance of 6.0 cm the base pressure was 5×10^{-7} torr. Using a more reasonable value of P=0.001, corresponding to a stoichiometric deviation of 0.1 at.%, a minimum pressure of 8×10^{-8} torr is required. These values are in agreement with the observations of many workers that a pressure of 10^{-7} torr was needed to obtain stoichiometric TiNi. At larger distances of 15.2 cm (6 in), the requisite base pressure was approximately 2×10^{-8} torr for P=0.01 and 2×10^{-9} torr for P=0.001.

Of particular interest is the strong dependence on the film stoichiometry with the target-sample distance at smaller distances. Only with low base pressures, and thus with P<0.001, can the film composition be ensured to be uniform over the wafer. Figure 2 then provides a guideline for chamber base pressures, which can then be related to the manufacturing compositional tolerances over a wafer, as well as providing a relationship between the target composition and sample composition.

2-3 Experimental Method

In order to control base pressure to levels of 1×10^{-8} torr, a UHV deposition system was utilized, as shown in Figure 2-3. A Perkin Elmer TNB-X series 1000 Pumping station and bell-jar, complete with a 300 l/s ion-pump was used to provide the pumping capability. Prior to deposition, the sample were washed in acetone, methanol and de-ionized water. Samples were then loaded onto an UHV compatible vacuum linear feed-through from a sample loading station. The sample and load-lock are pumped to 10^{-6} torr using a Leybold turbo molecular pump. In order to facilitate good removal of H_2O, this part of the system was illuminated with infrared irradiation to desorb water from the chamber walls without the danger of overheating and de-poling the sample transfer rod magnets.

The vacuum was analyzed using a Dycor RGA so that the composition of the atmosphere before and after sample insertion and after the Ar gas was leaked in could be recorded. As described in the previous section, this characterization is vital to determine the maximum sputtering distance. Titanium sublimation pumps (TSPs) were used to scrub residual water vapor and oxygen prior to the insertion of Ar. Due to the placement of the TSP by Perkin-Elmer, during deposition the ion-pump was isolated by a poppet valve in order to avoid pumping of the Ar. Thus, during deposition, the system is pumped by the Turbo pump only.

The sputtering methodology was as follows. Samples were introduced into the load-lock and pumped via the turbo-pump for 6 to 12 hrs prior to insertion into the deposition chamber. The load-lock was isolated by 1.5 in diameter gate valve and was opened to allow the sample to be inserted into the chamber. This method provided consistent base pressures, as measured by the RGA, prior to sputtering. Following a monitoring of the gas pressure, the ion-pump/TSP pumping well was then isolated and ultra-high purity Ar gas was leaked into the chamber. At a pressure of 10^{-4} torr, the content of the atmosphere was determined using the RGA and if acceptable, further Ar was leaked in to a final sputtering pressure of 2 to 4×10^{-3} torr. This pressure was monitored during

deposition using a Leybold gauge. The sputtering pressures were too high for RGA operation, and therefore it was not possible to monitor gas atmospheres during deposition.

The sputtering yields are generally low for this system, and therefore sputtering times are relatively long (approximately 30 min.) to deposit several microns of material. In order to avoid contamination during deposition, the turbo pump system actively pumped on the Ar during deposition. After deposition, the Ar is pumped out of the system and the vacuum analyzed to determine the contaminant level.

The basic deposition geometry is shown in Figure 2-3. Two MDX-1K DC sputtering sources deposited material at a predetermined wattage and time onto quartz samples. The target to sample distance was controlled by positioning the sample via the linear feed-through. No in-situ annealing was available in the chamber, and therefore the films were amorphous after deposition.

To best characterize systematically the effect of sample to target distance, and to avoid systematic errors involved in contamination in communal vacuum tube furnaces and with atmospheric interactions, a vacuum furnace mounted onto a manipulator was installed inside the chamber. The sample heater consisted of two 500W halogen lamps surrounded by a 3 in diameter half cylinder of polished stainless steel, to both focus the radiation onto the sample and to impede heating of the chamber walls, which would result in an increase in base pressure. A type K thermocouple was aligned so that the bead was 0.5 inch out from the plane of the halogen lamps using ceramic thermocouple tubing. Samples were pressed onto the bead during annealing, thereby ensuring that all samples were aligned similarly in annealing and allowing measurement of the sample temperature. The heater was controlled by a variac and the temperature measured using a Keithly Model 52 thermocouple meter. Typical annealing times were for 0.5 hr at 520 °C to 540 °C. As the thin-film is well lagged with respect to the sample holder, as the quartz substrate is relatively thick (2.5 mm), the sample temperature measured by the thermocouple is likely an accurate measurement.

After deposition and annealing, the sample was retracted through the vacuum load-lock and isolated from the chamber. The sample was allowed to cool for 1 hr. After shut down of the turbo and rotary pumps, the sample was removed for characterization. Upon exposure to air, the sample temperature was approximately 35°C.

2-4 Results

Generally, samples are introduced to the load-lock 12 hrs before sputtering, in order to minimize contaminants. Also the chamber pressure prior to the opening of the load-lock to the chamber was typically Typical base pressures were of the order of $2x10^{-8}$ torr. Measured gas compositions for the sputtering chamber are listed in Table 2-1, which demonstrates that the principal contaminants were N_2 and H_2O. When the load-lock was opened, there was little additional gas contaminants introduced, with the exception of H2, where an order of magnitude more gas was evolved, but which stabilized after further

pumping. The introduction of Ar did raised the total levels of reactive gas species. by a factor of 3, but still within acceptable limits of 10^{-9} torr. Finally after a deposition, these levels were not demonstrably lower or higher, indicating that the gas contaminant levels were likely stable during sputtering.

As this type of loading time is long, an investigation of the vacuum quality with a reduced loading time was performed. In this series of tests, the chamber had not been baked and so the base pressure was on the order of 10^{-7} torr. Samples were introduced to the load-lock 2 hr. prior to opening the system to the chamber. Table 2-2 summarizes the RGA analysis of the gas composition both during annealing and when the sample is being heated. With the ion pump closed and the chamber pumped by the Turbo pump, the gas pressures for contaminants was not measurably raised, even with the introduction of small amounts of Ar gas.

During sample annealing, the Ar supply is shut off but the system is still pumped with by the Turbo pump. After several minutes, the chamber walls exposed to the radiation were hot to touch. RGA analysis of the vacuum, displayed in the final column of Table 2-2, demonstrates that all contaminants are raised, especially N_2 and H_2O, as expected. However, as the sputtering deposition process is over, the only gas incorporation is through oxide and nitride formation on the surface. Visually, the samples look metallic, with no discernable blue or brownish tint, which is evidence of oxidation or nitridation respectively.

To investigate the influence of the sample to target distance, TiNi was deposited from a TiNi target which was made by powder metallurgy techniques in the author's laboratory. XRD analysis of the target was a mixed B2 and B19' microstructure.

Deposition was at 100 W for 1 hr onto quartz substrates followed by a 30 min. anneal at 540 °C, as measured by the thermocouple. Figure 4 shows the extent of the influence of sample to target distance on the microstructure of TiNi with good base pressure. At the limit of stroke of the magnetic manipulator, corresponding to a minimum target-sample distance of 8.0 cm, the XRD of the sample shows two peaks, corresponding to the TiNi's B2 [100] peak at $2\theta = 43.352$ (2.12A°) and a peak at $2\theta = 43.352$ (2.09 A°) possibly the B19 [020] peak (2.06 A°) phases, which are similar in composition to the target material. Precise phase identification of the B19' phase is problematic, due to the lack of additional peaks. This is not uncommon in TiNi as the martensitic B19' phase are generally highly textured. The only other phase which might be identified was Ti_4Ni_3, which also has a principal peak at 2.09 A°, and its existence cannot be conclusively ruled out.

At a distance of 10 cm and greater, the XRD profiles revealed only the B2[100] peak, with several small peaks at 2θ positions of 20.84°, 23.37°, 25.00° and 29.16°, corrsesponding to d-spacings of 4.24A°, 3.80 A°, 3.56 A° and 3.059 A°. No consistent identification could be made in ascribing these peaks as oxides of Ti, Ni or Ti-Ni. However. there was a reasonable identification of these peaks as harmonics of the B2 phase. in which the first peak is the second harmonic of B2<110> spacing of 2.12A°, the third peak is the second harmonic of B2<111> spacing of 3.56A° and the fourth peak is

the second harmonic of B2<200> spacing of 3.059 A°. The second peak may correspond to a plane spacings of √3 of the <110> planes. Neither first harmonic was observed for <200> or <111> planes, and thus this identification is plausible but not yet conclusive.

Beyond the target-sample distance of 10 cm, the only peak observed is the B2<110> peak, with no nitrification or oxidation peaks observed. At a limiting distance of 25 cm, the XRD profile had additional peaks corresponding to the likely formation of oxides and nitrides on the surface. At large sample to target distances (>20 cm), the thickness of thin film material deposited onto the sample was small, thereby decreasing the number of peaks observed and making a meaningful phase identification difficult.

The results are in general agreement with calculation, in particular at large distances. A sample to target distance of 10 to 15 cm, found in co-deposition or the sputtering of large area wafers, implies UHV conditions of 10^{-8} torr. Of interest is the change in XRD spectra between 8 cm and 10 cm. The compositional changes in the Ti-Ni ratio required to produce these changes are slight, which using a minimum value of P=0.001 would suggest that a total pressure of reactive species of $1x10^{-8}$ torr. As base pressures before sputtering were measured $3x10^{-8}$ torr, and a significant amount of Ar is subsequently introduced, there may likely be larger compositional differences.

2-5 Conclusions

For successful deposition of TiNi, the reactivity of the TiNi determines the maximum base pressures to be used. The agreement of the model with the calculation indicates that at a distance of 10 cm (4 in), the maximum base pressures that can be tolerated are of the order of 10^{-9} torr. Thus, UHV conditions are required for co-deposition of TiNi which then influences both the cost and throughput of fabrication of co-deposited TiNi devices.

The study has some implications for manufacturing. First, we have demonstrated that a powder metallurgy target can be used to provide TiNi samples which allows for a considerable amount of flexibility when compared to rod target. This was achieved despite the relatively porous nature of the target, and so the ability to generate such TiNi samples was interesting.

The extreme dependence of the thermodynamic properties of the system with composition suggests that sputtering distances and base pressures can be important to ensure that the resultant transformations will be uniformly similar for TiNi devices made from a wafer, regardless of the position of the material on the substrate.

UCLA Thin Film Deposition

1.1 Research Accomplishments

The response time of TiNi has been the subject of several experimental and theoretical investigations over the past decade. One of the principal concerns with this material is the relatively low cycle speeds or operational bandwidth associated with the cooling process. During

the last year we developed a finite difference model of heat transfer including the latent heat dissipated during the phase transformation to predict the bandwidth of thin film TiNi. The film was modeled as a plate subjected to either forced or free convection along the exposed surfaces and clamped to a large thermal mass representative of silicon wafer at the ends of the specimens. Results indicate that both latent heat as well as the relative ratios of the transformation temperatures to ambient temperature strongly influence the bandwidth of the material. Good correlation between the analytical model and test data obtained on a 38 micron wire indicate the model contains the correct assumptions to predict bandwidths. The bandwidth of TiNi thin film are predicted to be on the order of 100 Hz assuming that the transformation temperatures for the film are the same as the bulk material.

In addition to modeling, we began conducting studies associated with fabricating and patterning thin film TiNi structures. The thin film was sputtered with a magnetron sputtering system available in the UCLA clean room facility. X-ray diffraction studies on these film indicate they were of poor quality and probably due to both insufficient vacuum and low deposition rate of this existing sputtering system. While the sputtered films UCLA were ineffective as actuators, the material was utilized to evaluate etching approaches to fabricate thin film TiNi structures. Conclusions include that the amorphous film etches twice as fast as the crystalline structure. Furthermore, the film is attacked by oxide etchants like HF and a buffered oxide etch (BOE) and thus the sacrificial layers cannot be oxides but should rather be polysilicon or some kind of metalization layer. Bulk etchants like KOH and NaOH both attack the TiNi and probably the safest bulk etchant is TMAH.

To remedy the problem with the existing sputtering system, we began constructing a dedicated system in our lab. During the last year we submitted and were awarded a National Science Foundation Equipment grant to construct a dedicated TiNi sputtering system. This system is currently on line with the first films produced in March of 1997. In the following paragraphs we present some of the theoretical and experimental results generated during the last year.

In Figure 1, we present analytical results for thin film TiNi as a function of film thickness for three different transformation temperatures, that is $(M_s+M_f)/2$ = 33, 40, and 47°C. For film thickness of 4 microns, the bandwidths are 69, 52, and 29 Hz for samples with latent heat dissipated at 47, 40 and 33 °C respectively. For a film whose thickness is 1 micron, the bandwidths are 277, 212, and 119 indicating that simple extrapolations based on film thickness is inappropriate. Furthermore, even though the transformation temperatures were reduced linearly (i.e. 7 °C), the corresponding reduction in bandwidths were nonlinear. Based on the good agreement obtained between experimental and analytical results in our lab for a wire, the predictions presented in Figure 1 appear to be reasonable numbers but a few of comments are required. First, thin film TiNi typically is Ni rich which lowers the transformation temperatures of the material. As presented in Figure 1, small changes in transformation temperatures with respect to ambient temperature significantly influence the bandwidth (e.g. almost a factor of three for a shift of 14°C). Furthermore, the model does not account for any internal heat generation due to friction produced during transformation which could limit the bandwidth of the material.

In our etching studies, we found that NiTi film was etched at an appreciable rate by HF and BOE, two standard oxide etchants used in lithography. Comparison of their relative etch rates are plotted in figure 2. Concentrated HF and diluted HF both etched amorphous and crystallized NiTi at similarly fast rates. BOE etched both amorphous and crystallized NiTi at about 100A/min which was considerably slower than the 1000A/min rate on wet oxide. Diluted HF (12.5wt%) etched both crystalline and amorphous NiTi at a rate of about 5000A/min, while

concentrated 50wt% HF had rates of about 17,000A/min which is comparable to the etch rates on wet oxides.
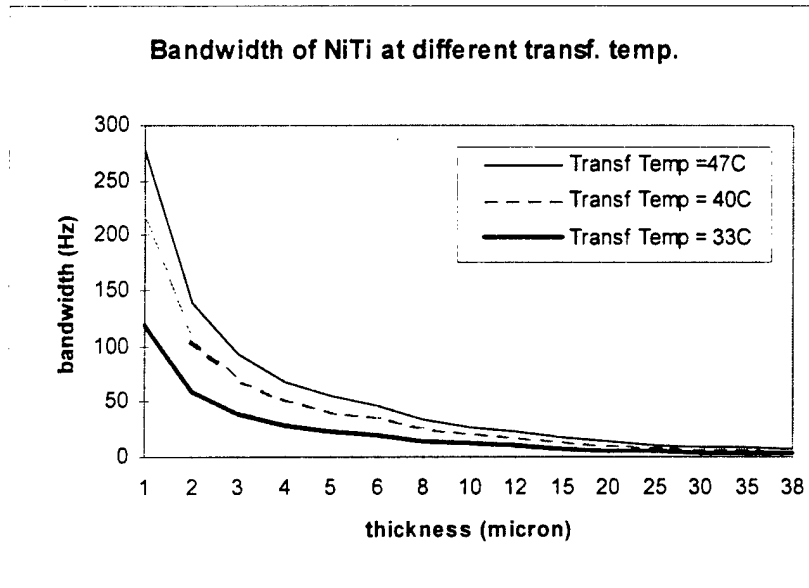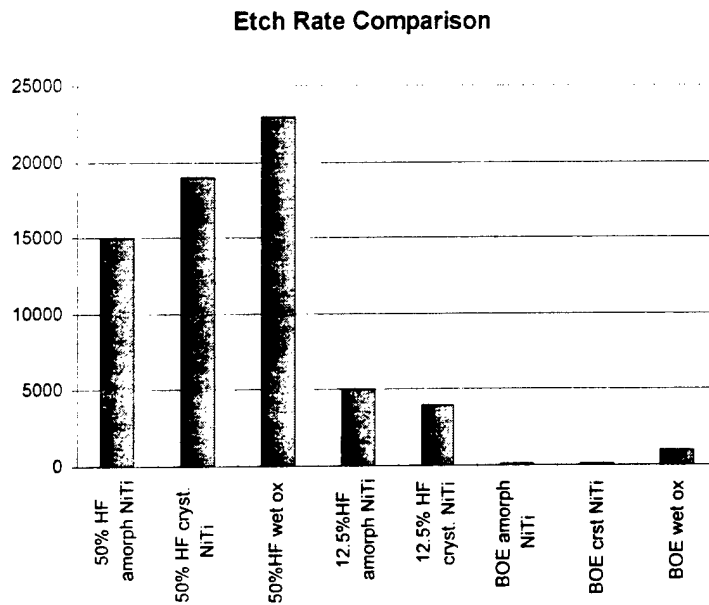
Bandwidth of NiTi at different transf. temp.

Figure 1:   Bandwidth for a thin film with three different martensite phase transformation temperatures.

Etch Rate Comparison

References

[2-1] J.Busch, A.D.Johnson, C.H.Lee and D.A.Stevenson,' Shape Memory Properties of Ni-Ti Sputter-deposited Film", J.Appl.Phys., 68:6224-6228 (1990)

[2-2] A.P.Jardine and L.D.Wasielesky,'Development of Thin Film Shape Memory Effect Nickel Titanium as Micron Sized Shape Memory Effect Actuators, Proc. M.R.S. Symp., 187:181-186 (1990).

[2-3] K.Ikuta, H.Fujita, M.Ikeda and S.Yamashita, "Crystallographic Analysis of TiNi Shape Memory Alloy for Micro Actuator", IEEE Micro Electro Mechanical Systems, 90CH2832-4:38-39 (1990)

[2-4] J.A.Walker, K.J.Gabriel and M.Mehregany, "Thin-film Processing of TiNi Shape Memory Alloy", *Sensors and Actuators* A21:243-246 (1990)

[2-5] S.Miyazaki and A.Ishida, Material Transactions, JIM, 35, p.14-10 (1994)

[2-6] B.Walles, L.Chang and D.S.Grummon,"Residual Stress, Adhesion and Crystallization of Ion-Sputtered and IBED processed NiTi Films", Proc. MRS Symp.246:349-354 (1991)
[2-7] A.P.Jardine, "Cycling Times of Thin-Film NiTi of Si", MRS Symp. Proc., "Shape Memory Materials and Phenomenon", 246:427-431 (1991)

[2-8] A.D.Johnson, "Vacuum deposited TiNi Shape Memory film: Characterization and Applications in Microdevices", *J. Micromech. Microeng.*, 1:34-41 (1991)

[2-9] K.N. Melton, "Ti-Ni Based Shape Memory Alloys", Engineering Aspects of Shape Memory Alloys, Butterworth-Heinemann Ltd, London, p21 (1990)

Figure 2-1: The variation of the TTR of TiNi with Changing Ti-Ni Stiochiometry. shown, changes in the Ti-Ni ratio can result in change of 100 °C in transformation temperatures. (All references to the data are contained in reference [9])

Figure 2-2: The variation of the maximum base pressure P_{cont} with sample-target distance. As seen, for most practical values of d, say at 6 cm, maximum base pressures range from 10^{-7} to 10^{-8} torr, with good stiochiometric uniformity over a substrate surface.

Figure 2-3: Schematic of the UHV sputtering apparatus. Not shown is the RGA which analyses the vacuum in the sputtering chamber. The sample was pulled along the plane of the deposition chamber using the linear feedthrough to vary the target to sample distance.

Figure 2-4: X-ray diffraction profiles taken for the TiNi samples with distance. At a sputter-target distance of 8 cm , peaks attributable to B2 and B19˚ phases were observed. At 10 cm to 20 cm, the B2 peak is observed, indicating low martenstic transformation temperatures. At 25 cm, B2 peak is difficult to identify and different peaks not associated with the transformation are observed.

Table 2-1: Typical gas compositions as measured by an Dycor M-1000 RGA unit in the sputtering chamber. In all four conditions, the total level of reactive gas contamination (P_{cont}) remains small.

Table 2-2: Gas compositions for a comparitively poor vacuum demonstrated reasonable insensitivity to pumping on closure of the ion-pump and uisng the turbo pump, or introduction of gas, thereby demonstating that gas contamination pressures are unlikely to be significant during deposition. During annealing, gas pressures are raised as the chamber walls desorb gas, however no oxide or nitridation was observed.
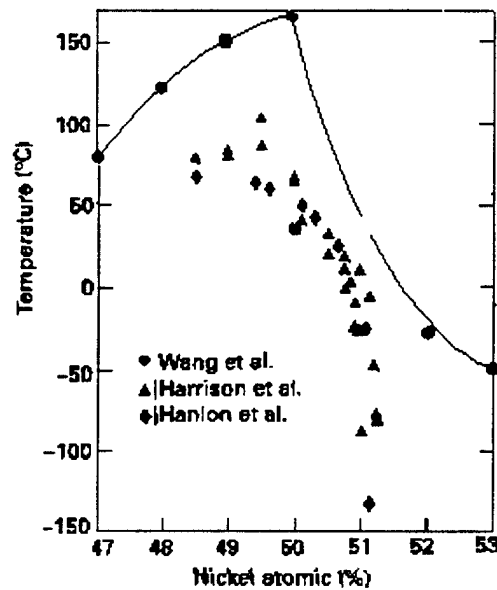
Figure 2-1

3- Thin Film TiNi/PZT Heterostructures:

Abstract

Thin film layers of shape memory alloys and ferroelectric ceramics can produce a family of 'smart' heterostructures capable of performing both sensing and actuating functions. Important issues in the synthesis of these active structures are the ability to generate the appropriate crystalline phases of each material while producing defect-free homogeneous high quality films. The compatibility of sol-gel processed $Pb(Zr,Ti)O_3$ (PZT) thin films with thin film shape memory effect TiNi substrates were investigated. Thin film TiNi was deposited on quartz substrates by physical sputter deposition utilizing a TiNi target in a ultra-high vacuum chamber, which was followed by in-situ vacuum annealing. The ferroelectric tetragonal phase of PZT was deposited on TiNi by sol-gel and spin coating processes followed a by 600 °C anneal for 5m in air. The heterostructures obtained were nominally defect-free, unlike those obtained through deposition onto bulk TiNi substrates.

J 5

3-1. Introduction

A material system is considered 'smart' if it has the ability to perform both sensing and actuating functions with some inherent control between these functions. Smart materials are categorized as either passive or active. Passive smart materials respond to external stimuli without any assistance, whereas active smart materials employ a feedback loop to initiate an appropriate response. A family of smart materials can be fabricated by depositing ferroelectric ceramics onto shape memory alloys (SMA). These hybrid structures couple the broad mechanical stress-strain hysteresis properties of SMA with the mechanical-electrical relationship associated with piezoelectric materials. These hetero-structures may have effective applications for active suppression of large acoustic waves.

Many alloys exhibit the ability to be deformed at low temperatures and regain their original undeformed shape when heated to higher temperatures. This phenomenon is known as the shape memory effect (SME) and is associated with dramatic changes in temperature dependent mechanical properties. It is due to a first order martensitic phase transformation from a high symmetry and high temperature *austenitic* B2 phase to a low symmetry and low temperature *martensitic* B19˙ phase. At the low temperature phase, the SMA is easily twinned into many crystallographic twin variants. Crystallographic twins grow at the expense of others with an applied stress. Macroscopically, the martensitic material is easily deformed through the growth of these twins, which can accommodate seemingly plastic strains (up to 8% for TiNi) that are recoverable upon heating.

Unlike most materials which display first order phase transformations, martensitic transformations demonstrate a transformation temperature hysteresis with a start and finish temperature for each transformation. The austenitic to martensitic transformation starts at a temperature denoted as M_s and finishes at a temperature M_f. The reverse transformation to the austenitic phase starts at A_s and finishes at A_f. In TiNi, the austenitic phase is a B2 bcc phase and the martensitic phase is a B19' monoclinic face-centered tetragonal structure. The transformation temperatures are very sensitive to the chemical stoichiometry of the alloy. Annealed TiNi can possess typical transformation temperatures of A_f =100 °C, M_f = °30 C , A_s=60 °C and M_s=50 °C, although these have to be characterized for each alloy. Compositional deviations of 1% Ni rich TiNi will dramatically lower the transformation temperature A_f to -100 °C [3-1].

The piezoelectric effect is the linear interaction between the electrical and mechanical systems of a material. An applied mechanical stress on a crystal produces a proportional electrical field known as the direct piezoelectric effect, whereas an applied electrical field produces a strain on the crystal known as the converse effect. There are a large number of ferroelectric ceramics, but the most widely researched and utilized for thin film technology are the titanates and niobates with the perovskite structure (e.g., lead zirconate titanate, lead lanthanum zirconate titanate, and barium titanate ($BaTiO_3$).

Coupling SMA and ferroelectric ceramics produces a hybrid composite structure that can utilize the different active and adaptive properties of the individual bulk materials. Ferroelectric ceramics are very sensitive to applied stresses through the piezoelectric effect. Their response times are fast, but displacements are very small (in the order of a few micrometers) due to the small strain magnitude. SMA materials have large actuation displacements and are able to drive larger loads. However, cycling times are much slower since it is dependent upon the dissipation of latent heat of transformation.

Smart active damping of mechanical vibrations is a possible application for these heterostructures. This requires the heterostructure to be able to sense the incoming stress wave and to actively respond. The logic of active damping by a ferroelastic-ferroelectric structure can be explained by considering an approaching stress wave shown in Figure 1. The stress wave propagates into the TiNi producing a martensitic-austenitic phase transformation in which some of the mechanical energy is converted to heat. This layer is designed to absorb most of the high energy waves. Acoustic waves that are not damped by the TiNi layer continue to propagate and strain the first ferroelectric layer (PZT). This strain produces a voltage through the direct piezoelectric effect which can be used to generate an out of phase stress wave by the second ferroelectric layer to attenuate any remaining stress waves. By varying the buffer layer (i.e., TiO_2) between the ferroelectric layers, it is possible to control the resistance and capacitance of the resulting circuit. To account for the possibility of the velocity of the stress wave to exceed the system's response time, a metallic mechanical impedance buffer (such as Al, Ti and TiNi) can be added to provide additional time for the counter-stress actuation to occur.

An important issue is the ability to generate the appropriate phases of each material while minimizing unwanted mutual chemical interactions. The amorphous crystalline transformation for TiNi occurs at 490-520 °C [3-2,3-3] and for temperatures above 540 °C, formation of Ti_3Ni_4 and $Ti_{11}Ni_{14}$ precipitates are favored which can be detrimental to SME characteristics. Decomposition of the ferroelastic phase of TiNi into $TiNi_3$ has also been observed by the authors to begin at 450 °C anneals with further decomposition at higher temperatures[3-4]. In contrast, annealing temperatures to transform amorphous

(sol-gel fabricated) ceramics to the ferroelectric perovskite phase range from 500 to 800 °C depending on the type of ferroelectric and at times the type of substrate[3-5,3-6,3-7,3-8,3-9].

TiO$_2$/PZT have been previously deposited onto TiNi by the authors and others through the sol-gel process with a crystallization temperature of 600 °C [3-4,3-10,3-11]. The objective of this experiment is to investigate the compatibility of PZT ferroelectrics with sputter deposited TiNi to improve the heterostructures mechanical and ferroelectric properties.

3-2. Experimental Procedure

An Advanced Energy MDX-1K DC sputtering source deposited TiNi from a TiNi target at a wattage of 100W for 1 h onto ambient temperature 25.4 mm (1") quartz substrates. The target to sample distance was controlled by positioning the sample via the linear feed-through, which varied from 8.5 to 26 cm. The TiNi deposition geometry and further details of the sputtering phenomena are discussed in an accompanying paper in this proceedings[3-12].

The thin films were initially amorphous and were annealed after deposition using a sample heater consisting of two 500W halogen lamps surrounded by a 76.2 mm (3") diameter half cylinder of polished stainless steel. Sample annealings were at 520 °C for 0.5 h. After deposition and annealing, the sample was retracted through the vacuum load-lock and isolated from the chamber. Following shut down of the pumps, the sample was removed for characterization.

The TiNi thin films did not receive additional treatment prior to PZT deposition. Thin films of PZT were coated onto SMA TiNi films by sol-gel and spin coating techniques. The complex alkoxide solution was prepared using lead acetate, zirconium n-propoxide and titanium isopropoxide metal alkoxides dissolved in acetic acid and 1-propanol alcohol. The PZT sol was prepared by dissolving 8 gm of lead acetate in 4 ml of acetic acid and heated to 105 °C (while being mechanically stirred) until solid form. After evaporation of all liquid, 4 ml of acetic acid was re-added and stirred for 15m. Appropriate amounts of Ti-isopropoxide was combined with Zr n-propoxide . The lead precursor was then added to the Zr/Ti precursor while being mechanically stirred. 40 ml of 1-propanol was added to the Pb/Zr/Ti precursor, followed by the addition of 1.0 ml of water to hydrolyze the solution. The general procedure is summarized in Figure 2. The PZT sol was filtered through a 0.22 μm filter before deposition onto substrates.

The PZT sol was spun onto the TiNi substrates at 4000 rpm for 30 s and prebaked at 300 °C for 15 m to remove most of the organics. This procedure was repeated (5 times) to produce thicker films. The PZT films were crystallized to their ferroelectric perovskite phase by annealing at 600 °C for 5 m. The samples were annealed on a ceramic block and allowed to air cool on the same ceramic block. This provided a slower cooling rate as compared to cooling the sample alone in ambient air. It is believed that by lowering the cooling rate, the TiNi intermetallic substrate and the PZT ceramic film composite will cool isotropically and inhibit large strain mismatch (which leads to cracking and delamination) due to linear thermal expansion behavior when rapidly air cooled. The films were characterized by x-ray diffraction (XRD) techniques, optical microscopy and a Radiant Technologies RT-66A ferroelectric test system was used to obtain ferroelectric properties.

3-3. Results and Discussions

<u>3-3.1 X-ray Diffraction Analysis</u>

Room temperature XRD of the TiNi thin films prior to PZT deposition and synthesis procedures demonstrated that the microstructure of the TiNi was largely the high temperature B2 phase. The transformation temperatures were not completely determined for this material, but some preliminary evidence showed an A_f = -10 °C and M_s = -40 °C, thus characterizing the mechanical properties of the thin film as superelastic rather than as thermally activated shape memory effect.

The diffraction pattern for the TiNi/quartz substrate after in-situ annealing at 520 °C anneals is shown in Figure 3-3a. The substrate was determined to be composed of superelastic austenite B2 phase of TiNi. Also present for the initial TiNi substrate diffraction pattern were 4 peaks that have not been conclusively identified at 2θ = 20.70°, 23.54°, 24.87°, and 29.18° (for CuKα radiation). The peaks were present before the TiNi substrate undergone sol-gel deposition, annealing or any other processing steps. These peaks seem to be some type of non-equilibrium oxide (Ti, Ni or TiNi) associated with the stock TiNi material that were not identified from the analysis of the JCPDS database.

The PZT film final thickness was approximately 0.28 μm for a 5 spin coat layer at 4000 rpm. The thickness of the films were measured by a Rudolph Research AutoEl II-NIR-3 ellipsometer and using a typical refractive index of 2.4 for PZT[3-13,3-14]. Room temperature XRD patterns were obtained for the PZT/TiNi and compared to the XRD of the starting substrate in Figure 3-3a and 3-3b. XRD analysis showed the presence of the

tetragonal perovskite phase of PZT as well as the B2 phase of TiNi. No other peaks were observed, thus indicating minimal chemical interactions took place between the two thin films. Of particular interest is the lack of any peaks associated with TiNi-air interactions. The Ti-air interaction at 600 °C is dramatic and very brief exposures (5 s) to high temperature furnaces will generate large amounts of oxides. The lack of peaks associated with Ti-O system suggests that the amorphous sol-gel film strongly attracts oxygen to form the ferroelectric oxide (which deprives the TiNi substrate to oxygen exposure). Further, the densified ceramic may well act as a diffusion barrier to further oxygen attack of the underlying TiNi metal. This explanation is supported by experiments on PZT/Pt and PZT/Al systems by Barrow and et al[3-15]. Their studies showed that crystallization of the amorphous ferroelectric film begins at the interface and nucleates towards the surface. They also observed reduced amounts of oxygen at the ferroelectric-metal interface which produces the cubic paraelectric PZT phase (near the interface).

3-3.2 Optical Microscopy

TiNi and PZT/TiNi film morphologies were characterized by optical microscopy. The sputtered TiNi films were atomically smooth, shown in Figure 4, with some semi-spherical features. The exact nature of these features are not currently known, but future experiments will be conducted to ascertain their cause.

The PZT film on the TiNi had a fine grain structure and exhibited no cracks over large areas. Optical micrographs at low and high magnification is illustrated in Figure 3-5. The lack of cracks is believed to be a result of the slowed cooling rate when the sample was left on the ceramic block to reach ambient temperature. Compared to samples prepared with commercially obtained bulk TiNi substrates, the sputtered TiNi films were atomically smooth. Experiments (pending publication) conducted by the authors showed that polished surfaces exhibited less cracking. Also, the sol was prepared differently from the past by diluting in a different alcohol and mixing order of precursors. This chemical modification of the sol may have reduced the evaporation rate of the gel, which has been known to greatly affect film quality during drying of sol-gel films.

3-3.3 Ferroelectric Characterization

Ferroelectric properties of the spin coated PZT films were obtained using a RT-66A ferroelectric test system by Radiant Technologies. A 1.0 µm diameter electrode was deposited on top of the PZT film using silver paint and the TiNi substrate was utilized as the bottom electrode. The tests were conducted under room temperature conditions

(20 C) with an applied 10V. A remanent polarization value of 0.152 μC/cm^2 and coercive field of -203 and 116 kV/cm were obtained for the 0.28 μm thick film. The capacitance and resistance were measured to be 0.52 nF and 6.2 x 10^{11} Ω-cm respectively. The hysteresis loop is illustrated in Figure 3-6. Typical P_r, P_s and E_c values for PZT are 23-30 μC/cm^2 , 45-50 μC/cm^2 and 40-45 kV/cm respectively.[3-16] The electrical values obtained for the PZT/TiNi are orders of magnitude different than typical values, but much better than values previously obtained by the authors for ferroelectric-ferroelastic systems[3-17]. It is believed that the low polarization and large coercive field values are due to problems associated with electrodes. The top electrode was painted onto the PZT substrate using a silver epoxy compound which was easily removed with pressure. The top electrode (Ag) differed from the bottom electrode material (TiNi) and therefore have different electron work functions. This could account for the difference between the -E_c and +E_c values. The large effects of electrode geometry, conductivity and material on the electrical values of the ferroelectric film have also been observed by others [3-18,3-19,3-20]

3-4. Conclusions

PZT thin films with a Zr/Ti of 53/47 were successfully crystallized onto thin film SMA TiNi. XRD patterns showed that the crystalline tetragonal phase associated with ferroelectricity was present after firing at a temperature of 600 °C for 5 m. XRD results also showed minimal chemical interaction with the B2 TiNi substrate and the perovskite PZT ceramic after annealing cycles. The PZT on TiNi had high mechanical qualities, showing lack of crack defects and strong adhesion with no signs of delamination. Ferroelectric properties were poor compared to literature values stemming from poor top electrode material and adhesion. However, polarization versus electric field plots reveal classical shape hysteresis loops, showing evidence of ferroelectricity.

References

3-1.　K. Otsuka, K. Shimizu, 'Shape Memory Materials', Proc. MRS Intl. Meeting on Advanced Materials (1988)

3-2.　J.D. Bush, A.D. Johnson et al, J. Appl. Phys., v68, p6224 (1990)

3-3.　J.S. Madsen and A.P. Jardine, Scripta Met et Metall., v30, p1189 (1994)

3-4.　P.G. Mercado and A.P. Jardine, 'Thin Film Multilayers of $TiNi/TiO_2/PZT$: Material Fabrication', SPIE Proc.: Smart Materials, Orlando Conference, v2189, p26 (1994)

3-5.　G. Yi, Z. Wu, M. Sayer, 'Preparation of $Pb(Zr,Ti)O3$ thin films by sol gel processing: electrical, optical, and electro-optic properties', J. Appl. Phys. 64 (5), p2717 (1988)

3-6.　C.K. Kwok and S.B. Desu, 'Pyrochlore to perovskite phase transformation in sol/gel
derived lead-zirconate-titanate thin films', Appl. Phys. Lett. 60 (12), p1430 (1992)

3-7.　C. Zhixiong, Z.Fangqiao, L. Meidong, W.Guoan and P.Xiangsheng, 'Sol-Gel Derived $BaTiO_3$ Ceramics', Ferroelectrics, v 123, p66 (1991)

3-8.　M.N. Kamalasanan, N.D. Kumar and S. Chandra, 'Dielectric and ferroelectric properties of $BaTiO3$ thin films grown by the sol-gel process', J. Appl. Phys., v 74 (9). p5679 (1993)

3-9.　Y. Suyama and M. Nagasawa, 'Synthesis of Single-Crystal Barium Titanium Isopropoxide Complex to Form Barium Titanate', J. Am. Ceram. Soc. v 77 (2), p603 (1994)

3-10.　A.P. Jardine and J.S. Madsen, 'Fabrication of "smart" ferroelastic-ferroelectric heterstructures', Smart Materials, V.K. Varadan, v1916, p384, SPIE, Alburquerque (1993)

3-11.　J. Chen, Q.C. Xu, M. Blaszkiewiez, R. Meyer, R.E. Newnham, 'Lead zirconate titanate thin films on nickel-titanium shape memory alloys: smarties', J. Am. Ceram. Soc., 75 (10), p2891 (1992)

3-12.　A.P. Jardine, 'Vacuum Conditions for Sputtering Thin Film TiNi', this proceeding

3-13.　C.H. Peng, J.F. Chang and S.B. Desu, 'Optical Properties of PZT, PLZT, and PNZT Thin Films', MRS Symp. Proc., Ferroelectric Thin Films II, v243, p21 (1992)

3-14.　C.H. Peng and S.B. Desu, 'Low Temperature Metalorganic Chemical Vapor Deposition of Perovskite $Pb(Zr_xTi_{1-x})O3$ thin Films', Appl. Phys. Lett., v61(1), p16, (1992)

3-15. D. Barrow, C.V.R. Vasant Kumar, R. Pascual and M.Sayer, 'Crystallization of Sol Gel PZT on Aluminum and Platinum Metallization', MRS Symp. Proc., <u>Ferroelectric Thin Films II</u>, v243, p113 (1992)

3-16. S.J. Lockwood, R.W. Schwartz, B.A. Tuttle and E.V. Thomas, 'Solution Chemistry Optimization of Sol-Gel Processed PZT Thin Films', MRS Symp. Proc., <u>Ferroelectric Thin Films III</u>, v310, p275 (1993)

3-17. A.P. Jardine and P.G. Mercado, 'Thin Film Multilayers of TiNi/TiO$_2$/PZT: Mechanical and Electrical Characterization', SPIE Proc.: Smart Materials, Orlando Conference, v2189, p37 (1994)

3-18. .S.P Faure, P.Gaucher and J.P Ganne, 'Influence of Geometrical Parameters on the Electrical Properties of Ferroelectric Thin Films', MRS Symp. Proc., <u>Ferroelectric Thin Films II</u>, v243, p129 (1992).

3-19. S.E. Bernacki, 'Polarization dependent Conductivity in Thin Film PZT Capacitors', MRS Symp. Proc., <u>Ferroelectric Thin Films II</u>, v243, p135 (1992).

3-20. D.J Eichorst and C.J., 'Effects of Pt Electrode Structures on Crystallinity and Electrical Properties of MOD-Prepared PZT Capacitors', MRS Symp. Proc., <u>Ferroelectric Thin Films III</u>, v310, p201 (1993).

FIGURE CAPTIONS

Figure 3-1: Schematic of a smart ferroelastic-ferroelectric active damping structure.

Figure 3- 2: Sol-gel processing of PZT films on TiNi.

Figure 3-3: XRD results of PZT/TiNi heterostructures: (a) initial TiNi substrate before any processing; (b) after firing at 600 °C for 5 m, demonstrating the existence of both TiNi (B2) and PZT (perovskite) phases..

Figure 3-4: Optical micrographs of TiNi films on quartz substrate showing smooth surface at 1000X magnification (marker =10 μm).

Figure 3-5: Optical micrographs of PZT films on TiNi/quartz substrates showing lack of cracks over large areas at: (a) 100X, marker =100 μm and; (b) 500X magnification, marker =50 μm.

Figure 3-6: Ferroelectric hysteresis plot for 0.28 μm thick PZT film on TiNi at room temperature with a P_r = 0.152 μC/cm^2.

TiNi

PZT

TiO2

Buffer (TiNi)

stress wave
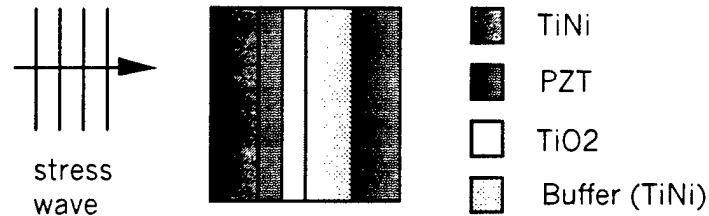
4-Porous TiNi Fabrication:

Commercially, the shape memory alloy TiNi is produced by either Vacuum Induction Melting or by Vacuum Arc Remelting of the pure metal ingots. Powder metallurgy techniques provide an alternative fabrication route but problems arise achieving chemical homogeneity. In this study TiNi compacts were cold pressed from the blended elemental powders and sintered in vacuum for varying times at temperatures from 800°C to 1000°C. Two heating rates were used, 5K/min and 10K/min. A TiNi microstructure could be produced after annealing at 1000°C for 6hrs, although some $TiNi_3$ was still observed. This is likely to be difficult to completely remove as $TiNi_3$ is thermodynamically more stable than TiNi. Thus, homogenization is unlikely to be completed by solid-state diffusion processes. The martensitic B19' structure was observed to be highly oriented after processing.

4-1 INTRODUCTION

There are many alloys exhibiting shape memory properties however TiNi possesses excellent mechanical properties and good corrosion resistance along with room temperature transformation temperatures, a large recovery force on heating and a long cyclic lifetime. Consequently, it has become the most commercially important of the shape memory alloys. Conventional synthesis of SME TiNi by either Vacuum Induction Melting (VIM) or Vacuum Arc Remelting (VAR) of the pure metals is costly. The transformation temperature M_s is strongly dependent on chemical composition and multiple remelting is required to minimize the presence of impurities and to achieve homogeneity. The difficulties in working and mechanically machining TiNi also add to the high cost and limit the commercial availability of this material to wire and sheet stock. Powder metallurgy can provide near-net shape processing that minimizes the need for machining however this has not been adequately explored as there are few commercial sources for TiNi powders. The purpose of this investigation was to

determine whether TiNi shape memory effect (SME) material can be produced from Ni and Ti elemental powders by powder processing and subsequent heat treatment.

4-2 POWDER METALLURGY

There are several synthesis problems that need to be considered. The first is the need to obtain a homogeneous TiNi alloy by interdiffusion while avoiding the formation of other intermetallics. An examination of the phase diagram[4-1], seen in Figure 1, reveals two neighboring stable intermetallic phases, $TiNi_3$ and Ti_2Ni. Further, there may also be metastable intermetallics such as Ni_3Ti_4 or $Ni_{11}Ti_{14}$ that can further complicate analysis[4-2]. The Gibbs free energies of the stable intermetallic phases, Ti_2Ni and $TiNi_3$, are lower than that for TiNi (see Table 4-1). Once formed, therefore, it is unlikely that these phases will entirely disappear. Many people[4-3—4-8] have obtained a mixture of the intermetallic phases TiNi, Ti_2Ni and $TiNi_3$ from the elemental powders via the PM route but the goal of homogeneous TiNi would seem to be difficult to achieve.

The second problem has been the need to eliminate porosity to improve the mechanical integrity of the actuating material. A major influence on the final sintered density is the initial green density which will increase with compaction pressure. In addition, Aksenov et al [4-3] and Igharo and Wood[4-5] both noted that while increasing the sintering temperature led to diffusional

	TiNi	Ti_2Ni	$TiNi_3$
ΔH°_f KJ/mol [9]	-66.6	-83.7	-140.3
S°_f J/Kmol [9]	53.2	83.6	104.6
C_p J/Kmol [9]	$39.1 + 39.5 \times 10^{-3}$ T	$61.2 + 49.6 \times 10^{-3}$ T	$73.1 + 98.5 \times 10^{-3}$ T
ΔG (800°C) KJ/mol	-159.0	-225.0	-325.9
ΔG (900°C) KJ/mol	-172.8	-245.6	-354.2
ΔG (1000°C) KJ/mol	-187.3	-267.1	-384.1

TABLE 1 : Calculated ΔG values for the stable Ti-Ni intermetallic phases.

homogenization it also led to a growth in diffusional porosity. This was due to Kirkendall void formation resulting from the difference in the diffusivity of the Ni and Ti elements (Ni diffuses faster than Ti)[4-10]. Furthermore high temperature sintering of inhomogeneous material can lead to the melting of compositions of low melting point

(m.p.)[4-5]. This liquid may be used to drive a densifying front through the entire sample as in the reactive sintering process[4-11]. However this phenomenon was not observed either by Igharo and Wood or by Morris and Morris who both associated liquid formation with the presence of large pores[4-5,4-6]. A plausible explanation has been suggested by Morris and Morris who point out that for liquid to form in this system it is necessary that solid state interdiffusion occur to form the required low m.p. composition. As the liquid phase forms at certain locations, other regions of better or poorer interdiffusion will remain solid, thus creating a solid skeleton phase and inhibiting the free particle movement that is necessary for densification improvement. Instead, the liquid is drawn by surface tension forces to fill the nearby fine porosity leaving behind large pores. Consequently, Morris and Morris state that priority must be given to achieving chemical homogeneity while avoiding the conditions where liquid is formed. A reduction of the scale of chemical inhomogeneity should allow easy solid state homogenization and so avoid any melting.

Finally it must be remembered that when TiNi is formed from the elemental mixture, its temperature rises rapidly by the heat of formation. Furthermore, the formation reactions of Ti_2Ni and $TiNi_3$ from their elements are also exothermic. The temperature rise together with the formation of the eutectic liquid (24.5at% Ni) may cause the deformation or the loss of the original compact shape and the formation of large pores. Kuroki et al[4-7] demonstrated that slowly heating from 550°C to 900°C at 2K/min can control the compound-forming reaction and resulted in good preservation of the compact shape. The heating rate for the compact was changed from 10K/min only in the reaction temperature range thus saving time while preserving the shape and dimensions.

EXPERIMENTAL DETAILS

The nickel and titanium powders, 99.9% and 99.5% pure respectively, and both 44μm, were combined in the ratio 50/50 atomic %. They were mixed by ball-milling, in a ceramic chamber for four hours. The specimens were then compacted in a uniaxial die press under 27.5 MPa for 5 minutes. The compacted specimens were 29 mm in diameter and typically 3.5 mm thick. The compacts were heat treated in a 10^{-6} torr vacuum tube furnace for varying times at temperatures ranging from 800 to 1000°C. Two heating rates were used: a slow heating rate of 5K/min and a faster heating rate of 10K/min. The green and sintered densities were determined from weight and dimensional measurements. The surfaces of the specimens were ground and a Phillips PW 1729 diffractometer was used to determine the phases present. Some specimens were subsequently sectioned and the cross-sections examined in an ISI-SX-30 scanning electron microscope using backscattered electrons.

The alloy is an ordered intermetallic equiatomic compound. It has a high temperature austenitic, cubic B2 phase and a low temperature, martensitic B19' phase that is

monoclinic. The TiNi (B19') and Ti$_2$Ni phases were identified on the basis of both SEM and XRD analysis, as XRD alone is ambiguous. The intermetallic phases all exhibit diffraction peaks very close to each other. In particular the TiNi$_2$ and B19' TiNi can be difficult to distinguish. The B19' phase has its main peak at 2θ =41.4°, a 94% peak at 2θ =45.0° and additional peaks at 39.3°, 44.0° and 45.2°. The Ti$_2$Ni phase has its principle peak at 2θ =41.6° plus peaks at 39.1° and 45.5°. Furthermore TiNi$_3$ has a peak at 43.7° and Ni has its principle peak at 44.5° making phase identification difficult, solely on the basis of XRD.

4-3 RESULTS

Slow heating rate (5K/min)

Shown in Figure 4-2 are XRD powder patterns for isochronal sintering for 12hrs in vacuum at various temperatures. At 800°C Ni, Ti, B2 (TiNi), Ti$_2$Ni and TiNi$_3$ peaks were present. No B19' (TiNi) peaks could be distinguished but it is possible that they were present yet masked by other peaks. As the temperature was raised above 800°C the elemental peaks decreased and the intermetallic peaks increased. At 900°C B19' peaks were seen, although the (111) peak at 2θ=45° was not observed until 1000°C. Figure 3 shows the XRD patterns for isothermal sintering at 1000°C for various times. After 1hr Ni was observed along with TiNi$_3$ and both the TiNi phases although the B19' (111) peak was not present. As sintering time increased the Ni and TiNi$_3$ peaks decreased until at 12hrs only TiNi$_3$ was present with TiNi. The 1000°C-6hr and 1000°C-12hr samples both showed orientation effects. In some orientations the sample exhibited the B19' peak at 2θ =45° and in others it did not.

Porosity was found to vary significantly with sintering temperature. SEM examinations of cross-sections taken at 800°C-12hr (Figure 4-4) found the pores to be much smaller (typically 25μm) and less interconnected than the 900°C or 1000°C samples. The microstructure was very smooth, i.e. contained no micro-voidage. The contrast in the backscattered mode indicates the different phases: TiNi, Ti$_2$Ni, TiNi$_3$, Ni and Ti, with the darkness of the phase corresponding to a larger Ti content. Porosity increased after sintering above 900°C. The 900°C-6hr and 1000°C-1hr microstructures were very open and contained large interconnected pores typically 80$\square$m in diameter (Figures 4-5a and 4-5b). Much of the material contained voidage and appeared "sponge-like" in character. This phase had an average composition from EDAX of 49.8at% Ti and was identified as TiNi. The sample also contained dense, "non-spongy" regions of TiNi along with small areas of TiNi$_3$ and Ni particles. The microstructures of the 900°C-24hr sample (Figure 4-6) was slightly more connected and continuous than the 6hr sample but still contained

large pores ~ 65μm in size. In both the 900°C-24hr and the 1000°C-12hr samples the sponge-like skeletal microstructure had been replaced by denser TiNi regions exhibiting fine voidage. Small regions of TiNi$_3$ remained but no Ni particles were observed.

Fast heating rate (10K/min)

Figure 4-7 shows the XRD patterns for the samples heated at 10K/min. After 6 hours at 900°C, B19', B2, TiNi$_3$, Ni and Ti peaks were present. However the sample showed an orientation effect with the B19' (111) peak at 2θ=45° present in some orientations and not in others. Furthermore the intensities of the (111) peak and the (101) peak at 2θ=39.3° varied greatly with sample orientation (Figure 4-8). After 6 hours at 1000°C the elemental peaks were no longer observed, and the B19', B2 and TiNi$_3$ peaks remained. The B19' (111) peak was always present but the intensity variation of this peak with sample orientation was still seen.

SEM analysis showed that the 1000°C-1hr microstructure was slightly more contiguous than the sample heated at the slower heating rate but still contained large pores approximately 50μm in diameter (Figure 4-9). The sample had no sponge-like microstructure but much of the TiNi phase appeared dendritic in character (Figure 4-10). EDAX analysis revealed that the sample contained Ti$_2$Ni, seen in the SEM micrographs as a dark gray phase. This phase was not seen in the slow heating rate samples, nor was a Ti$_2$Ni peak seen in the XRD pattern although it is possible that it was masked by the larger B19' peaks. EDAX analysis confirmed the presence of TiNi, TiNi$_3$ and Ni.

4-5 DISCUSSION

Densities

The mean green densities were not very high, being only about 65% of the theoretical density, 6.44g/cm^3. This is due to the comparatively low compaction pressure of 27.5MPa. This low green density results in a low sintered density. The sintered densities were all lower than the green densities, typically 60%. This has been observed before by Igharo and Wood[5] and could be due to the effect of Kirkendall voidage on sintering. A slight increase in sintered density was seen for the compacts heated at the higher rate but the effect was not significant.

Microstructures

The results demonstrate the difficulty of performing phase analysis on the basis of XRD alone. Initial XRD analysis of the 900°C samples and the 1000°C-1hr specimen

identified the peaks at $2\theta=38.9^{\circ}$, 41.4°, and 45.2° to be Ti_2Ni on the basis of d values and intensity measurements. SEM observations and EDAX analysis however, did not reveal any phase with 66.7at%Ti composition. The peaks were therefore identified as B19', despite the fact that the peaks at $2\theta=44^{\circ}$ and 45° were not present.

An orientation effect was seen to be associated with the B19' (101) and (111) peaks at $2\theta=39.3^{\circ}$ and 45°, especially at higher sintering temperatures ($1000^{\circ}C$) and higher heating rates (10K/min). In some orientations these peaks were seen, in some they were not, and in some orientations the intensities were very high. It is obvious that some of the crystals were aligning in preferential directions during sintering. This is surprising since the stress on the compact should be low; the initial compaction pressures were comparatively low and at such temperatures any stresses should be relieved. Furthermore the samples were furnace cooled so no cooling stresses should have developed.

Slow heating rate (5K/min)

As the sintering temperature increased, the pore size was observed to increase. The pore size of the $800^{\circ}C$ sample was much smaller than the $900^{\circ}C/1000^{\circ}C$ samples ($25\mu m$ as opposed to $75\mu m$). Igharo and Wood[5] noted a gradual fall in density with increasing sintering temperature which became dramatic as the temperature was raised to $1000^{\circ}C$. They attributed this to the formation of a transient liquid phase of a eutectic composition (24.5at% Ni). Although this eutectic temperature is $>900^{\circ}C$ the formation of the intermetallic phases from their elemental components is an exothermic reaction and local temperatures could be higher than the furnace temperature. The increase in pore size seen at $900^{\circ}C$ is therefore probably associated with the formation of a liquid phase. As proposed by Morris and Morris[4-6] this large-scale porosity is probably due to the liquid being drawn away by capillary action to fine voids, leaving behind large pores. At $800^{\circ}C$, however, it is probable that the formation reactions did not generate enough heat to melt the constituents and that little formation reaction was occurring due to poor solid state diffusion.

SEM examination revealed that many of the samples sintered at $900^{\circ}C$ and $1000^{\circ}C$ contain a "spongy", skeletal structure with a composition that corresponds to TiNi. Closer examination of this phase showed voids separated by a skeletal network of TiNi. The most likely explanation for this voidage is that is Kirkendall porosity due to the difference in Ni and Ti diffusivity. The sponge-like structure was not seen at all in the $800^{\circ}C$ sample; the microstructure contains no micro-voidage. This is likely to be because insufficient interdiffusion had occurred for Kirkendall voidage to develop. As the temperature and sintering time increased the spongy structure in these samples became a denser structure containing fine voids. This is in accordance with the above theory that as sintering time and temperature increase a liquid phase is formed that is drawn away by surface tension forces to the surfaces of fine voids. Thus the micro-

voidage decreases. Some voidage is also present in the $TiNi_3$ phase although much less than is in the TiNi phase. However this phase tends to be slightly deficient in Ni (approximately 73at% Ni), again, further evidence that the Ni atoms diffuse faster than the Ti atoms.

From the SEM micrograph the 800°C-12hr sample appeared inhomogeneous with Ti, Ni, Ti_2Ni, $TiNi_3$ and TiNi present. At 900°C and 1000°C, however, the samples appear well mixed with most of the material present as TiNi. After 24hrs at 900°C or 6hrs at 1000°C, few Ni particles remained and the sample was mainly TiNi with a few small areas of $TiNi_3$. Since $TiNi_3$ has the smallest Gibbs free energy of all the stable intermetallic phases at 1000°C it is unlikely that this phase could be completely removed by solid-state diffusion.

High heating rate (10K/min)

There is no evidence of the sponge-like TiNi phase that is present in the slower heating rate samples however the phase is dendritic. It is likely that the higher heating rate resulted in greater heat being generated by the exothermic intermetallic formation reactions. More material would thus be melted than at the slower heating rate leading to a more cast-like TiNi structure. SEM observations and EDAX analysis of the 1000°C-1hr sample revealed the presence of Ti_2Ni along with TiNi, $TiNi_3$ and Ni. A look at the phase diagram (Figure 1), however, reveals that Ti_2Ni should not exist at 1000°C. This phase was not seen in the slow heating rate samples however, and as the heating rate is raised the system will be increasingly non-equilibrium. However the sample appeared to be well mixed with the majority of the structure being TiNi and after holding for 6hrs at 1000°C XRD indicated that the Ni had vanished.

These results are in contrast to Zhang's study[4-8] who achieved mostly TiNi with a few small areas of $TiNi_3$ after sintering for 5hrs at 900°C. XRD indicates that the 900°C-6hr sample in this study, (10K/min heating rate), still contains Ni along with TiNi and $TiNi_3$. However Zhang's study used initial heating rates of 20K/min to 600°C and 10K/min to 700°C and a final heating rate of 2K/min to 900°C. It is evident from this study that heating rate greatly affects the types of phases formed and the resultant morphology.

Thermodynamics

Since the compacts are formed from the elemental powders, the formation of Ni-rich and Ti-rich phases is unavoidable if only solid-state sintering is used. The Gibbs free energy calculations (Table 4-1) show that TiNi is the least stable of the three equilibrium,

intermetallic phases and that $TiNi_3$ the most stable. When sintering begins then, $TiNi_3$ is likely to be the first phase to form. This formation reaction is strongly exothermic. As sintering continues the sample will equilibriate and TiNi will form if the overall composition is 50/50 atomic%. XRD analysis and SEM/EDAX observations indicated that the Ti-rich phases, Ti and Ti_2Ni disappeared before the Ni-rich phases. This is to be expected if the Ni atoms diffuse faster than the Ti atoms. The Ni atoms will diffuse toward the Ti atoms, eliminating the Ti-rich areas but the Ti atoms will be slower in moving toward the Ni-rich atoms. For the stoichiometry to be correct, however, the TiNi phase(s) must be slightly Ti-rich. This was not found to be the case; on average the TiNi phase was Ni-rich. However the $TiNi_3$ phase was found to be slightly Ni deficient. Obtaining a final equilibrium structure of TiNi alone by solid-state diffusion is unlikely since $TiNi_3$ has the smallest Gibbs free energy of all the stable intermetallic phases and is therefore more stable than TiNi.

A more complete discussion will be found published in reference (4-12).

4-6 CONCLUSIONS

At 900°C-24hrs and 1000°C-6hrs, heating at 5K/min, the samples were mainly homogeneous TiNi with little Ni remaining and only small regions of TiNi$_3$. Thermodynamic calculations indicate that the presence of TiNi$_3$ is unavoidable if only solid-state sintering is used to homogenize the sample since this phase is the most stable of the intermetallic phases.

The heating rate appears to have a significant effect on both the phases formed and on the resultant morphology. Increasing the heating rate appears to decrease the microvoidage present and at much greater rates might lead to densification through reaction sintering. However raising the heating rate also increases the likelihood of introducing non-equilibrium phases.

There is a strong orientation effect associated with the B19' 2θ=39.3° and 45° peaks, especially at higher sintering temperatures (1000°C) and higher heating rates (10K/min). In some orientations these peaks were seen, in some they were not, and in some orientations the intensities were very high. Presumably some of the crystals were aligning in preferential directions during sintering. Further investigation is required to explain this phenomenon.

5-Summary

In conclusion, we were successful in demonstrating that the various interfaces and specialized material components could be synthesized successfully. We were not able to build the entire ensemble however, due to the personnel changes initiated at Stony Brook, which forced a redirection of the remaining funds.

However, the knowledge base has been developed to allow this to happen and for both an analytical and modelling effort, as well as an experimental effort to go forward. This research and development program would most likely be a 6-2 to 6-3 applied R&D effort, and should be directed at a small company SBIR in conjunction with ARL.

(6) List of all publications and technical reports

1. Jardine, A.P., "Vacuum Conditions for Sputtering Thin Film TiNi," *Journal of Vacuum Science and Technology A*, **13(3.1)**; pp 1058-1062, May-June, 1995.

2. Mercado, P.G. and Jardine, A.P., "Smart Thin Film TiNi/Piezoelectric Heterostructures," *Journal of Vacuum Science and Technology A*, **13(3.1)**, pp. 1017-1021, May-June 1995.

3. Mercado, P.G., Jardine, A.P., "Development of Thin Film TiNi/Pb(Zr,Ti)O$_3$ Heterostructures," Proc. of the SPIE, **2441**, Smart Structures and Materials 1995, February 27-28, San Diego, CA, pp. 419-427.

4. Mercado, P.G. and Jardine, A.P., "Smart Thin Film TiNi/PZT Heterostructures," Proc. Materials for Smart Systems Symposium, E.P. George, S. Takahashi, S. Trolier-McKinstry, K. Uchino, and others, Eds., Pittsburgh, PA, November 28-30, 1994, pp. 419-427.

5. 'Dynamical Response of Thin Film Shape Memory Effect TiNi Cantilevered Beams', P.G.Mercado and A.P.Jardine (submitted, **Sensors and Actuators A**)

6. 'Thermo-Mechanical Properties of Thin-Film NiTi Deposited on Si", A.P.Jardine, (submitted "**Smart Materials and Structures**")

7. "Synthesis and Characterization of TiNi-Ferroelectric Heterostructures" , **invited paper**, (submitted, **J.Intell. Materials and Structures**)

8. ' Analysis of the Superelastic Damping Mechanism in Cored TiNi material', A.P.Jardine, (submitted, **J.Material Science**)

9. "Synthesis and Characterization of PZT Microballoons", (submitted, **Materials Letters**)

10. 'TiNi Synthesis from Elemental Powder Components' , by Janet C. Hey and A.Peter Jardine, (to be published, SPIE Conference Proc., (1994))

11. 'Thin film Multilayers of TiNi-PZT (I): Fabrication and Characterization', Peter G Mercado and A.Peter.Jardine, (to be published , SPIE Conference Proc., (Feb 1994))

12. 'Thin film Multilayers of TiNi-PZT (II): Mechanical and Structural Properties', Peter G Mercado and A.Peter.Jardine, (to be published, SPIE Conference Proc., (Feb 1994))

13. Ho, K, Carman, G.P., Jardine, P., Kim, C.J., "Modeling and Measuring the Response Times of Thin film TiNi," Smart Structures and Materials 1997 Smart Materials Technology, San Diego 1997, pp. 10-23.

3 5

(7) List of all participating scientific personnel showing any advanced degrees earned by them while employed on the project:

3)   Peter Mercado:M.Sc.
4)   John Madsen:M.Sc
5)   Janet Hey:M.Sc
6)   Ken Ho, M.Sc " "Modeling and Measuring the Response Times of Thin film TiNi," March 1997, University of California Los Angeles.
7)   Greg P. Carman, Professor, UCLA
8)   Peter Jardine, Asst. Professor, SUNY SB
9)   John Parise, Professor, SUNY SB

(8) Report of Inventions (by title only)

• Ferroelastic-Ferroelectric Heterostructures: US Patent No.

(9) Bibliography

(10) Appendixes